Artificial Intelligence Chemistry 1 (2023) 100028

Contents lists available at ScienceDirect

Artificial Intelligence Chemistry

journal homepage: www.journals.elsevier.com/artificial-intelligence-chemistry

Machine learning and robot-assisted synthesis of diverse gold nanorods via seedless approach

Oyawale Adetunji Moses [a,b,1], Mukhtar Lawan Adam [a,c,1], Zijian Chen [a,d,1], Collins Izuchukwu Ezeh [d], Hao Huang [e], Zhuo Wang [a,d], Zixuan Wang [a], Boyuan Wang [f], Wentao Li [a,d], Chensu Wang [a,d], Zongyou Yin [g,*], Yang Lu [h,*], Xue-Feng Yu [e,*], Haitao Zhao [a,*]

[a] Center for Intelligent and Biomimetic Systems, Shenzhen Institutes of Advanced Technology, Chinese Academy of Sciences, Shenzhen 440305, China
[b] Huaxi MR Research Center (HMRRC), Department of Radiology, Functional, and Molecular Imaging Key Laboratory of Sichuan Province, West China Hospital of Sichuan University, Chengdu 610041, China
[c] Physics Department, Bayero University, Kano 700231, Nigeria
[d] Department of Chemical and Environmental Engineering, The University of Nottingham Ningbo China, Ningbo 315100, China
[e] Materials Interfaces Center, Shenzhen Institute of Advanced Technology, Chinese Academy of Sciences, Shenzhen, Guangdong 518055, China
[f] Department of Physics, University College London, Gower Street, London WC1E 6BT, UK
[g] Research School of Chemistry, Australian National University, ACT 2601, Australia
[h] Department of Mechanical Engineering, The University of Hong Kong, Pokfulam Road, Hong Kong, China

ARTICLE INFO

Keywords:
Machine learning
Robotic synthesis
Nanomaterial synthesis
Data-driven approach

ABSTRACT

The challenge of data-driven synthesis of advanced nanomaterials can be minimized by using machine learning algorithms to optimize synthesis parameters and expedite the innovation process. In this study, a high-throughput robotic platform was employed to synthesize over 1356 gold nanorods with varying aspect ratios via a seedless approach. The developed models guided us in synthesizing gold nanorods with customized morphology, resulting in highly repeatable morphological yield with quantifiable structure-modulating precursor adjustments. The study provides insight into the dynamic relationships between key structure-modulating precursors and the structural morphology of gold nanorods based on the expected aspect ratio. The high-throughput robotic platform-fabricated gold nanorods demonstrated precise aspect ratio control when spectrophotometrically investigated and further validated with the transmission electron microscopy characterization. These findings demonstrate the potential of high-throughput robot-assisted synthesis and machine learning in the synthesis optimization of gold nanorods and aided in the development of models that can aid such synthesis of as-desired gold nanorods.

Introduction

Recently, data-driven materials innovation constitutes emerging interdisciplinary fields of automation [1–4], big data [5] and artificial intelligence (AI)[6,7] with tremendous potential and advantages. Lately, machine learning (ML) is progressively materializing as a practical package adaptable to materials research [8–10], thus enhancing scientific insights and chemical intuition [11]. However, the lack of materials database with proper descriptors/features restricts further development [12,13]. The growing demand for advanced materials spurs the development of a high-throughput experimental (HTE) system that can overcome such bottlenecks. One of the promising solutions is a robot-assisted HTE platform, which can be utilized to minimize error-prone experimentation and expedite the acquisition of feature data. Therefore, the advanced Human-AI-Robot collaborative approach has attracted considerable interest in the development of data-driven materials synthesis to probe into the complex dynamic relationship happening in the nanomaterial synthesis process [14–16].

Robotic [17,18] or automatic [19,20] experiments play an increasingly prominent role in the advanced materials development processes. Over the past decades, tremendous efforts have been made to use computers for scientific instrument control and data acquisition, which

* Corresponding authors.
E-mail addresses: zongyou.yin@anu.edu.au (Z. Yin), ylu1@hku.hk (Y. Lu), xf.yu@siat.ac.cn (X.-F. Yu), ht.zhao@siat.ac.cn (H. Zhao).
[1] These authors contributed equally to this work

https://doi.org/10.1016/j.aichem.2023.100028
Received 22 July 2023; Received in revised form 31 October 2023; Accepted 17 November 2023
Available online 19 November 2023

is considered the beginning of automated laboratories [21–23]. Anticipatedly, in order to propel the conventional physical experiments towards data-derived automation, computational models, academic software, and data-mining codes have been attempted [24–26]. Nowadays, following empirical, theoretical, and computational science paradigms, data-driven science is showing tremendous potential in material science [27,28]. A universally programmable chemical synthesis machine [19,20] and a robotic chemist [29] are the benchmark of full automation for materials research. In particular, advances in AI [6,7], big data [5,30,31], automation [2,4,32] have presented a wealth of opportunities in the emergence of materials digital synthesis. Resultantly, a data-driven synthesis is evolving, requiring a systematic approach that combines the merger of ML, robotic HTE platforms, and datasets in materials discovery [27,33].

Here, we show how it is possible to integrate ML and robotic HTE platforms with the generated database for the data-driven synthesis of diverse gold nanorods via a seedless approach. Notably, we choose noble metal plasmonic nanoparticles such as gold nanorods (Au NRs) with dynamic target properties. The plasmon resonance tunability inevitably depends on adjustability of Au nanoparticles [34,35], which precisely dictates the extent of diversified applications in surface-enhanced Raman scattering [36–40], sensors [41,42], biotechnology [43,44], and energy [45,46]. Therefore, a thorough investigation involving robotic high-throughput manipulation of Au NRs aspect ratio (AR) and optical density ratio (OD ratio) becomes necessary, culminating in a valuable conclusion capable of guiding the predictable synthesis of as-desired Au NRs. Methodologically, we chose the concentration of the reactants identified as structure-modulating precursors (SMP) for the robotic HTE platform as the primary features, with the optical disposition of the as-synthesized Au NRs as the target property. Then, we utilized the sure independence screening and sparsifying operator ML algorithm [47,48] to search for optimal multi-dimensional descriptors/expressions by scanning the synthesis chemical space [49,50]. The models extracted herein can be utilized as prior surrogate models for expanded synthesis or as optimized models for understanding the quantitative role of experimental conditions in synthesis processes. Considerably, the integrated machine learning and robot-assisted synthesis of diverse gold nanorods from this study will serve as an archetypal system for shape control of similar optically-inclined nanocrystals, capable of spearheading innovations of materials digital synthesis.

Results and discussion

Workflow of machine learning and robot-assisted synthesis

Compared to manual synthesis, automation using a reconfigurable robotic HTE platform has accorded high-quality experimental endpoints in the parallelized synthesis of diverse Au NRs via a seedless approach, as an orthogonal array and single-feature combinatorial experimental design were executed. Here, the critical strategic principle is to discern the optimal combinatorial (with high accuracy prediction) of the primary features from an immensity of pre-collected datasets. Subsequently, the combination of multiple features (via robotic HTE platform-generated datasets) is employed to generate accurate data diversified enough to train machine learning models, which can serve as an archetypal system for digitizing materials fabrication and minimizing ambiguous errors associated with manual syntheses.

As shown in Fig. 1, the workflow involves five design schemes. The first is the design of experiment (A), which involves adapting orthogonal arrays to scheme the numerical inputs containing reactants ratio/concentration. Thus, aiding the choice of specific concentration levels for the single-feature (SF) technique, which was then transcribed into the interface of the robotic HTE platform (B) to perform high-throughput synthesis of Au NRs. wherein, the parts of synthesis process performed by the robot including diluting the prepared standard solutions, synthesizing Au nanorods, shaking the reaction solution and capturing color images. The open and close of the spectrometer's doors, and the measurement of the spectrometer have been also operated automatically. Further training and analysis using the ML model (C) were adopted to predict the sample quantitative and qualitative optimization – visualized through UV-Vis absorption spectra, which aided the newly designed double- and triple-features (DF and TF) techniques (D). Finally, the model is validated with further experiments and characterizations (E).

More than 1300 experiments were performed as local gradients, along which the reactants' concentrations varied. Thus, reliability of the

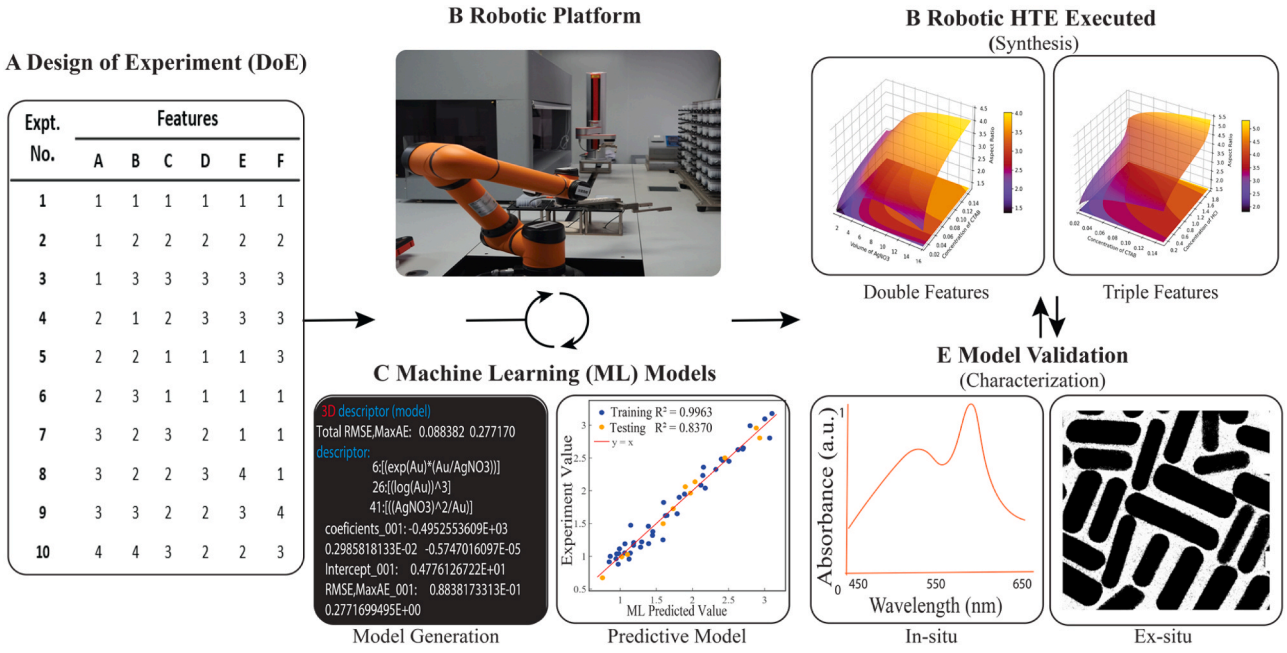

Fig. 1. The workflow of machine learning and robot-assisted synthesis of diverse Au NRs. (A) The design of experiments. (B) The robotic HTE platform. (C) Machine learning-assisted synthesis models generation (R^2 of Training set: 0.9963, R^2 of Testing set: 0.8370). (D) Robotic HTE platform-executed synthesis with double- and triple features. (E) Model validation through in-situ (UV-Vis) and ex-situ (TEM morphological) characterization.

executed experimental outputs was ensured by observing their optical dispositions, in terms of UV absorption spectra of Au NRs growth solution. Moreover, color captures of some growth samples mounted on robotic HTE platform were obtained, and few were strategically selected for TEM characterization.

Robotic synthesis equipped with orthogonal and combinatorial experimental design

For decades, statistical methodologies in design of experiments have been utilized for the optimization of nanomaterials properties [51]. This study inculcates algorithms and statistical models to analyze and draw inferences from patterns in the synthesis data of Au NRs. Our promising alternative begins with the robotic HTE synthesis platform using an orthogonal array model for optimal property discovery and combinatorial approaches for complex pattern recognition of the feature space through ML models. Herein, a similar technique and conditions were adopted to synthesize Au NRs and rationally secure their comparison.

An orthogonal array experiment ($L_{18}(3)^6$) was used and the boundaries of the parameters space were selected based on combination of prior literature and preliminary trial and error experiments to determine the optimal formulation needed for pinpointing the most viable SMPs in further combinatorial experiments (Table S1). Similarly, a UV–vis spectrophotometer was utilized to keep track of the Au NRs' shape and size modulation, synthesized using the robotic HTE platform (see *SI appendix* for every experimental data obtained). Table S2 highlights different results from the orthogonal array experiments, which were concurrently synthesized thrice in parallelization by the robotic HTE platform to ascertain reproducibility, as revealed in (Fig. 2(A)) - a visual testament to the reliable performance of such robotic HTE platform and the different colors represent varying outcomes of Au nanorods nucleation process after 2-hour period, following orthogonal experimentation. This has ascertained the possibility of controlling the Au NRs AR through variation of precursors concentration ratios. The absorption spectra of some orthogonal array experiments, as shown in Fig. 2(B-D), indicate diverse transverse and longitudinal surface plasmon resonance (TSPR and LSPR, respectively) absorption at lower and higher infrared regions. While Fig. 2(B) indicates that results obtained from orthogonal array experiments somehow lack the necessary correlation between TSPR or LSPR and SMP for deciding the best out of all other feasible SMP adopted for this seedless Au NRs synthesis, Fig. 2(C-D) affirms the reliable repeatability of the growth solutions.

However, the question remains: which reactants play the most prominent roles in actively adjusting the aspect ratio? Also, which of the 18 robotic HTE platform-executed experiments expresses the highest viability for further examination regarding high Au NRs yields, quality, and lesser by-products? Perhaps, a critical investigation and much further extension of experiments will bring significant clarification to these questions. A thorough assessment indicates that orthogonal array experiment 9 exhibits a level of supremacy above the rest, in terms of high Au nanorod yields, without compromising the purity level (highest OD ratio) [52], and thus shall further serve as the adjustable default to be utilized for proceeding experimentations.

Ordinarily, such a lack of much-needed sequence in the above-detailed orthogonal array experiments can be obviated using combinatorial approaches. The solutions brought about by using a robotic HTE platform to screen composition–structure-property relationships via combinatorial approaches trump the conventional Edisonian approach that employs tweaking one parameter at a time. Resultantly, enough datasets can be generated for training ML modeling, and then ideal SMP quantities can be precisely pin-pointed toward optimal yield. Leveraging the robotic HTE platform to cover the entire experimental design space, we apply the SF combinatorial approach that involves a default use of optimal values associated with this model, although with an increasing variation in a feature (concentration-wise). As shown in Table S3, the ensuing one-dimensional growth of Au NRs with a similar trend in AR and OD ratio reveals the innate ability of CTAB to act as a modulating precursor. This might be because Br ions contained in CTAB actively affix to the [100] and/or [110] facets of the Au growth post-nucleation, rather than closely-packed face-centered-cubic structures at their opposite ends [53], as the former boasts of abundant surface energy more than the latter [54].

Such cruciality of maintaining CTAB concentration above critical micelle concentration (1 mM) has been severally emphasized [55], which is reflected by the optical changes in the growth colloids above this stated benchmark [56] - the plasmon shift steadily increases with decreasing CTAB concentration (Fig. 2(E)). Similarly, the amount of gold salt increases the ratio of gold ions to other precursors increases, as more will be distributed towards the longitudinal frame, thereby increasing the AR up until they become inundated, which could have led to an increase in fractionally reactive remnants, as evidenced by the declining AR and OD ratio (Fig. 2(F); Table S4).

At the outset, with an increasing volume of 0.01 M $AgNO_3$ in the growth solution, a fast-paced formation of high Au NRs AR occurred, until a threshold was reached at a volume of 12 μl, after which AR increase became insignificant, coupled with diminishing nucleation (OD ratio) of Au NRs (Fig. 2(G), Table S5). This may be attributed to the interaction between silver ions and the bromide counterion of the CTAB monomers [57]. Unlike some multi-step seeded growth processes where pH increment is ineffective on LSPR [58], the seedless synthesis results indicate otherwise, significantly influencing AR and OD ratio (Fig. 2(H); Table S6). Possibly, this might be due to the indirect influence of HCl on ascorbic acid (AA), whose reducibility of Au ions depreciates with dwindling pH and hence slower growth pace, which culminates into higher AR [59]. Hence, we classify the precursors mentioned above as the SMPs, unlike the other three precursors (NaOL, AA, and $NaBH_4$) with less pronounced effects on the Au NRs AR and OD ratio, visibly reflected in the camera-captured color images and spectrophotometric data of each growth product (Figure S1; Table S7-S9).

Machine learning-assisted synthesis models generation and evaluation

The experimental datasets were modeled using the compressing sensing method [47,48]. This enables us to generate suitable nonlinear expressions linking Au nanorods' structural descriptors (AR or OD ratio) and the synthesis descriptors (concentration/volumetric/molarity of SMPs) from the pool of generated datasets. In this scenario, the method explores and exploits the model associated with the most accurate synthesis recipe capable of describing the dynamics between the selected target features (AR or OD), thereby highlighting the primary features closely related to synthetic consequences. Following the selection of the most significant synthesis descriptors, a combination of these parameters can be used to predict the optimal SMPs and combinatorial ratio within the given synthesis condition. Ab initio, as presented in Fig. 3(A-F) and Fig. S2, is a correlogram illustrating the feature-feature correlation between the selected primary features from the DF and TF experimental datasets, respectively. This is to check-mate the existence of highly correlated features in the synthesis space. From the correlogram of the 64 DF, in each of the experiments the features interact considerably as-anticipated. However, the influence of certain feature one feature is more dominant to the other in all the cases. Such is the cases in all other synthesis space of the TF experimental datasets.

Furthermore, the ML prediction and detection of the optimal SMPs and combinatorial ratio are harrowing from the single-feature experiments due to the multi-dimensional precursor-response dependence. To address such shortcomings, the complementarity of the ML-assisted robotic HTE synthesis platform offers an excellent solution in the further extension of experiments to accommodate multiple features such as double-features (DF) and triple-features (TF) (to be discussed) in the determination of optimized synergized effects of suitable Au NRs SMPs. Two features (DF) and three features (TF) from the combinations of the selected primary features (C_{AgNO3}, C_{CTAB}, C_{HAuCl4}, and C_{HCl}) are used to

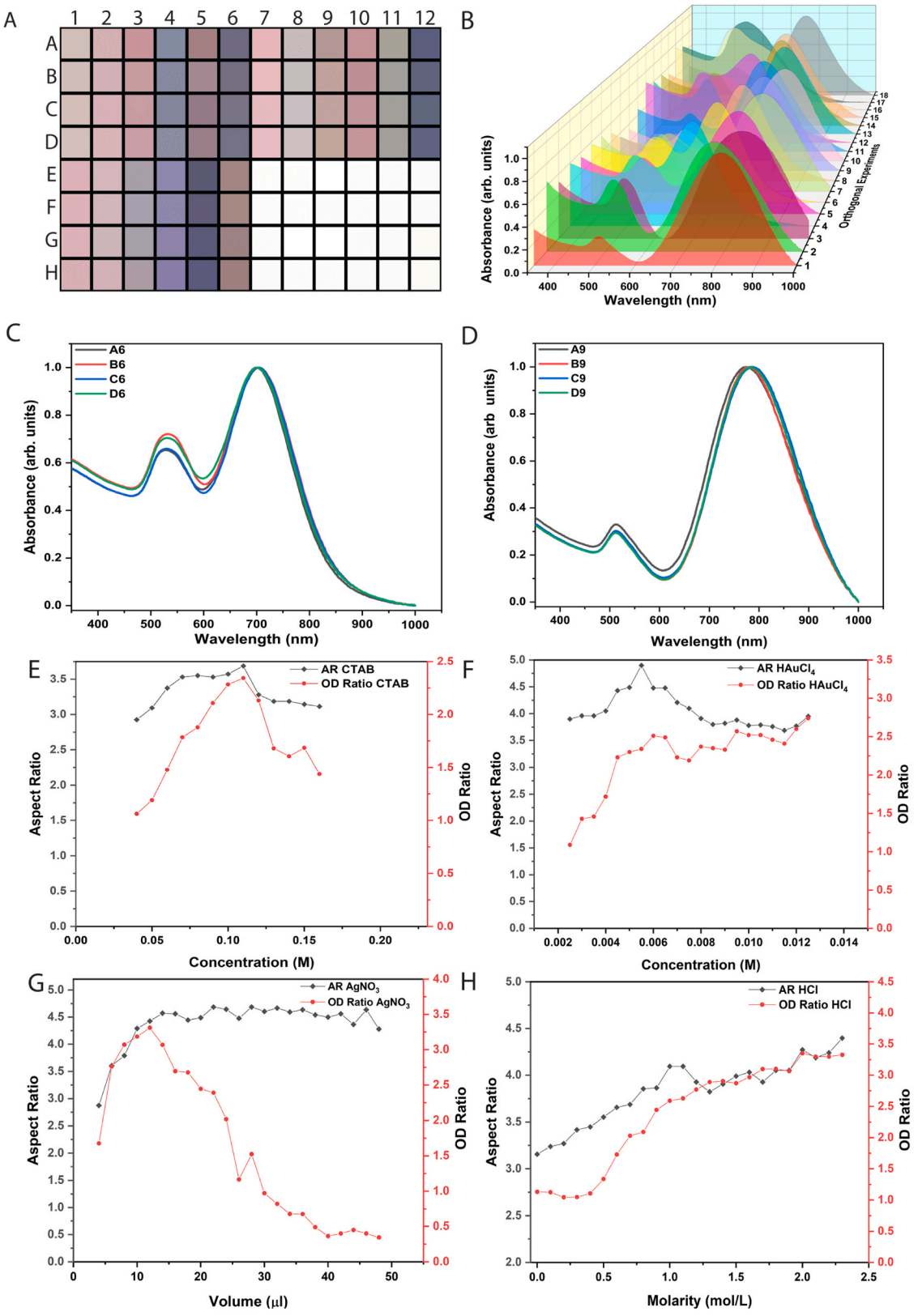

Fig. 2. Orthogonal Au nanorods synthesis via robotic HTE platform; (A) Simulated image following 2 h of Au nanorods nucleation, with each experiment replicated three (3) more times. (B) Normalized UV absorption spectra of as-prepared Au growth solution of entire orthogonal array experiments, indicating the transformation of both TSPR and LSPR, based on different precursors molarities. (C-D) Orthogonal array experiments 6 and 9, respectively, indicate the repeatability of the as-prepared growth solution. Aspect ratio and optical density ratio obtained from combinatorial experimental design, depicting variation spanning 24-: concentration levels of (E) CTAB (F) $HAuCl_4$, (G) volumetric levels of 0.01 M $AgNO_3$ and (H) molarity levels of HCl.

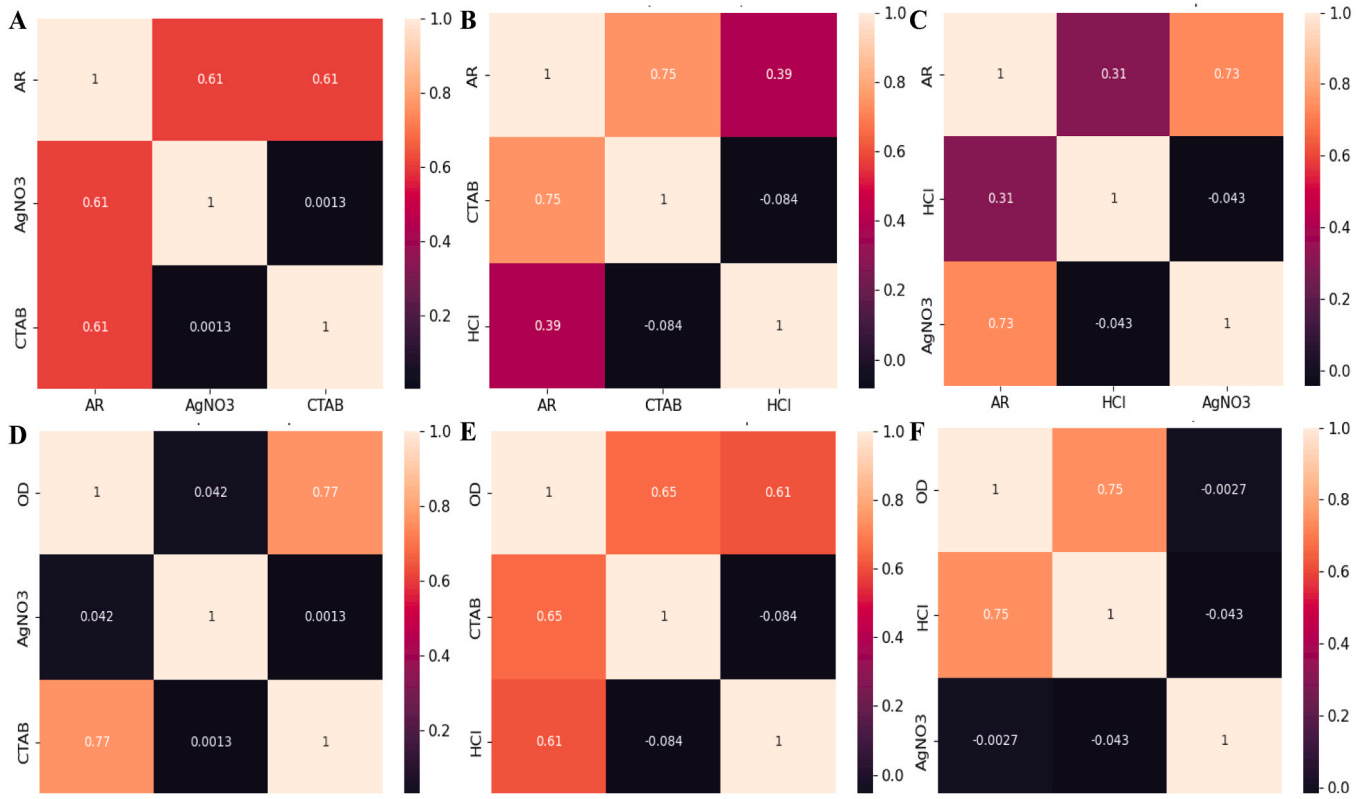

Fig. 3. Correlogram illustrating the correlation index between the primary features for structure modulating precursors extracted from the 64 double-features experiments, relating to AR in (A) $AgNO_3$/CTAB, (B) CTAB/HCl and (C) AR in $HAuCl_4/AgNO_3$; and OD ratio in (D) $AgNO_3$/CTAB, (E) CTAB/HCl and (F) $HAuCl_4/AgNO_3$.

construct the features space Φ_0, using four binary operators (+, -, x, /) and five unary operators ($^{-1}$, ^{2}, ^{3}, exp, log), on the feature space. These generate considerable numbers of secondary features for DF and TF in Φ_3 after three iterations. However, more complex models can be constructed through further iteration of the feature space.

In our case, the dataset's training errors are generally reduced in the Φ_2 and Φ_3 spaces. Hence, further iterations beyond the Φ_3 space will overfit the dataset without significantly improving the accuracy of the generated models. The experimental dataset for training the ML models was further enlarged from 64 to 96 in both the DF and TF experiments to ascertain the predictive performance of the algorithm, which is tested beyond the training data. The models were further examined using a hypothetical dataset, shown in the ML model visualization (to be further discussed), in understanding the dynamic role of the primary features relative to the target feature (AR or OD ratio).

For the generated model evaluation, the chosen expressions were based on low root-mean-square error and the number of terms in the expression. For example, Eqs. (1) and (2) show the chosen model of the AR and OD, respectively, from 64 training datasets of the DF experiment with the lowest RMSE of 0.1139 and 0.1190. The models for the remaining datasets of the DF and TF experiments are all presented in Tables S10-S17 of the supporting tables.

$$Y^i_{AR} = C^i_1\left(\log(C_{CTAB})\left(C_{AgNO3}\right)\right)+C^i_2\left(C_{AgNO3}/\exp(C_{AgNO3})\right) + C^i_3\left(\left(C_{AgNO3}-C_{CTAB}\right)\left(C_{AgNO3}/C_{CTAB}\right)\right)+C^i_0 \quad (1)$$

$$Y^i_{OD} = C^i_1\left(\left(C_{AgNO3}-C_{CTAB}\right)\left(C_{CTAB}/C_{AgNO3}\right)\right)+C^i_2\left(C_{CTAB}C_{AgNO3}/\exp(C_{AgNO3})\right) + C^i_3\left(\left(C_{AgNO3}\right)^3/\left(C_{CTAB}+C_{AgNO3}\right)\right)+C^i_0 \quad (2)$$

Further on, we revalidate the performance of the expression using random forest regression, as implemented in scikit-learn in predicting AR and OD ratios. For the quantitative performance evaluation, we used the metrics of RMSE and Coefficient of Determination (R^2) between the target and predicted values for each task, as shown in Fig. 4. Smaller values of RMSE (< 0.1) and larger values of R^2 (> 0.95) indicate the reliability of the models (Details of R^2s and RMSEs in Tables S54). The results (Figs. 3 and 4) indicate that the models can predict and establish accurate relationships between the SMPs and the Au NRs AR and OD ratios. This result demonstrates the reliability of the models generated from the symbolic regressor, which employs advanced algorithms to uncover intricate patterns and connections within complex datasets, enabling a deeper understanding of the intricate interplay between the SMPs and the AR/OD ratios of the Au NRs. By leveraging the symbolic regressor's capabilities, we are able to extract nuanced insights that may not be discernible through conventional statistical methods alone. Moreover, the reliability of the models underscores the consistent and trustworthy nature of the connections established by the symbolic regressor, which are rooted in substantial statistical significance and are validated through rigorous testing procedures. Fig. 4, S3-S4 show the experimental and predicted values parity plots for 64-DF, 64-TF, and 96-TF experiments, respectively. With sure independence screening and sparsifying operator and random forest regression machine learning algorithms-assisted synthesis model generation, it is possible to minimize the time and resources dedicated to the "trial and error" experimental optimization process when Au NRs with the desired AR or OD ratio properties are needed for specific applications. At the same time, ambiguous assumptions or inferences in data interpretations are eliminated.

Robotic HTE platform-executed synthesis with double-features

The optimal region of the experimental design space is not necessarily restricted to a point. It can thus be elucidated by ML model

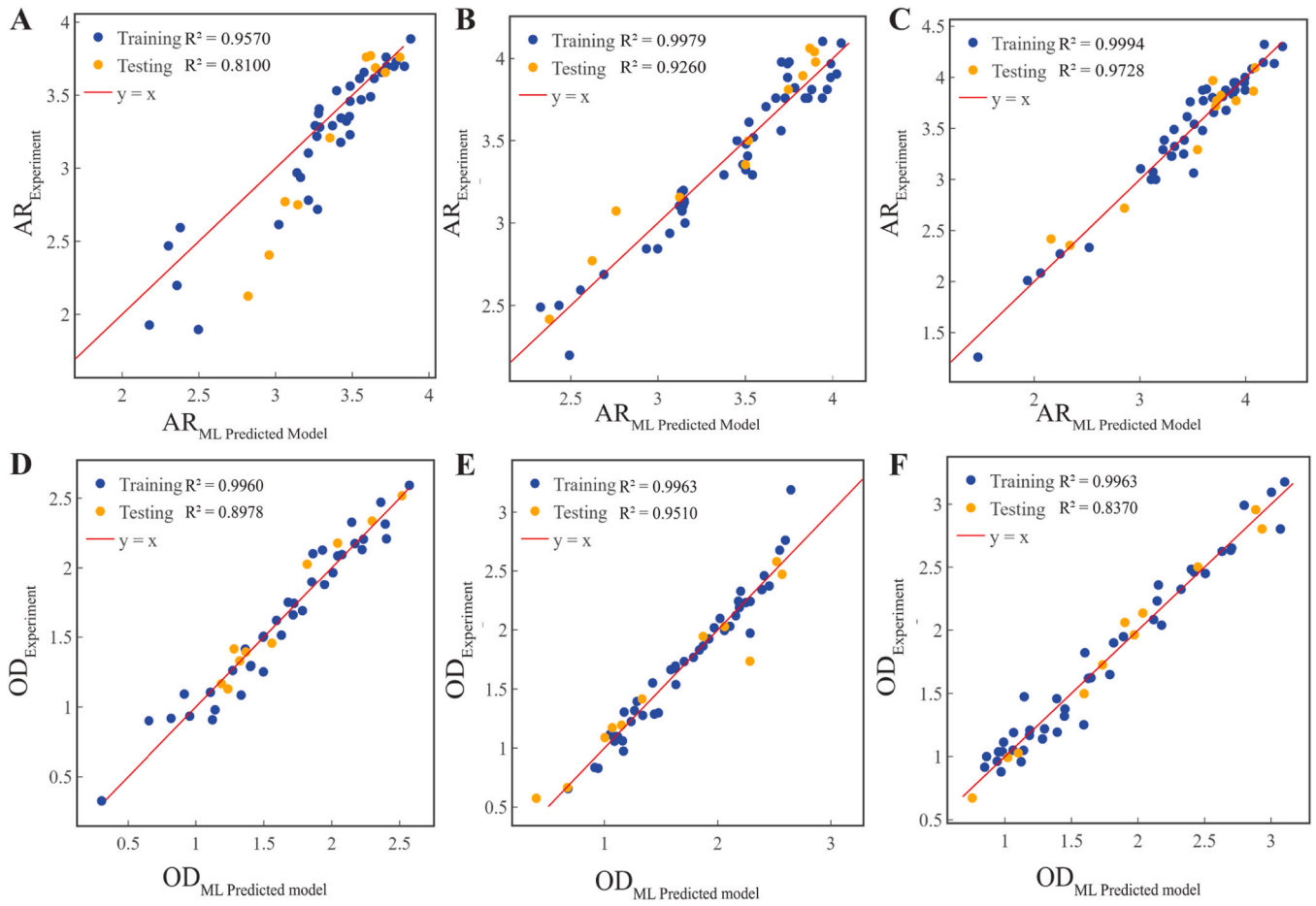

Fig. 4. The model prediction accuracy measured by the correlation coefficient (R^2) and root mean square error (RMSE) between observations and predictions of the structure modulating precursors on Au NRs, classified by AR in (A) $AgNO_3$/CTAB, (B) $HAuCl_4/AgNO_3$ and (C) CTAB/HCl; and OD ratio in (D) $AgNO_3$/CTAB, (E) $HAuCl_4/AgNO_3$ and (F) CTAB/HCl, for the 64 double-features experiments.

visualization of the robotic HTE platform-executed experimental datasets in identifying the best domain of applicability without the need to test every possible point. Thus, double-features combinatorial enables further generation of training datasets necessary for accurate ML model predictions. To justify this approach, we juxtapose the synergistic influence of SMPs, visualized through ML-based color mapping, with the corresponding robotic HTE platform-executed experimental datasets (tabulated in the supporting information). Sufficient to say that SF resized Au NRs, as it encompasses adjustments in width-dependent TSPR peak positions analogous to LSPR, only when key SMP were varied (Fig. S5(A-D)), while insignificantly in other features (Fig. S6(A-C)) [60]. But the ingenuity brought about by ML-assisted synthesis modeling and robotic HTE platform-driven DF technique is meant to selectively resize Au NRs of desired and optimal quality, involving precursors input with precision. Thus, the beforementioned SMPs (CTAB, $HAuCl_4$, $AgNO_3$, and HCl) are varied in pairs to fine-tune Au NRs AR, even toward the maximum possible values. Majorly the SF region associated with steady AR growth was initially chosen in 64 concentration experiments. The resulting datasets are comparable to the ML-modeled color map and the projected overview in Fig. 5(A-E).

Observations from robotic HTE platform-executed DF experiments indicate the synergistic influence of CTAB and $HAuCl_4$ on Au NR outputs (Table S18). The maximal Au NRs AR were prominent in the region with low gold salt but high CTAB concentration levels (Fig. 5(A)). Specifically, results shown in Table S19 confirmed the introduction of low $HAuCl_4$ content (0.003 M) into a diverse reaction mixture containing 0.085, 0.1, and 0.115 M CTAB concentration, similarly generating the same maximum AR of 4.33. This result emphasizes the role of CTAB in the growth solution. Silver ions, for their parts, have reportedly been one of the significant contributors in shape alterations [61,62] and optical demonstration [63] of Au nanoparticles. Parenthetically, for $HAuCl_4/AgNO_3$ datasets tabulated in Table S20, there is an improving trend with increasingly introduced silver ion contents detected, with high stability across both low and high concentrations from both reactants, highlighting the relevance of fixed proportion of Au/Ag ions ratio needed for Au NRs formation (Fig. 5(B)). The ML model backs this up with high accuracy ($R^2 > 0.9$, RMSE < 0.03) in Fig. 4(B), the as high disparity in the proportion of Ag to Au ions could diminish the prospect of Au NR genesis (Table S21(B)), where the presence of $AgNO_3$ having high volumetric molarities of 9, 11, 13, and 15, produced no LSPR growth solution containing meager 0.001 M solution of $HAuCl_4$.

Furthermore, the robotic HTE platform-executed Au NRs experimental DF datasets from $HAuCl_4$/HCl (Table S22) indicate an observable trend from progressive input of HCl that stimulated a meteoric surge in Au NRs AR, which was enhanced with an increase in gold salt content (Fig. 5(C)). As noted in Table S23, the range of Au NRs with peak AR falls in the region of high HCl molarity coupled with relatively low $HAuCl_4$ concentration. Pivotal structural modulating effects of $AgNO_3$/CTAB as designed in Table S24 were brought to the fore and discerned to be well-matched, such that they required a balanced proportion to attain remarkable output [64]. The results in Table S25 and high R^2 (> 0.95) shown in Fig. 4(A) confirm the consistency between the observations and ML model predictions. As inferred, following nucleation, AgBr–ions impede the growth of the Au nanoparticles, thereby ensuring a parallel growth to the planar direction, creating increasingly elongated Au NR structures in the process. However, it was noted that extending the

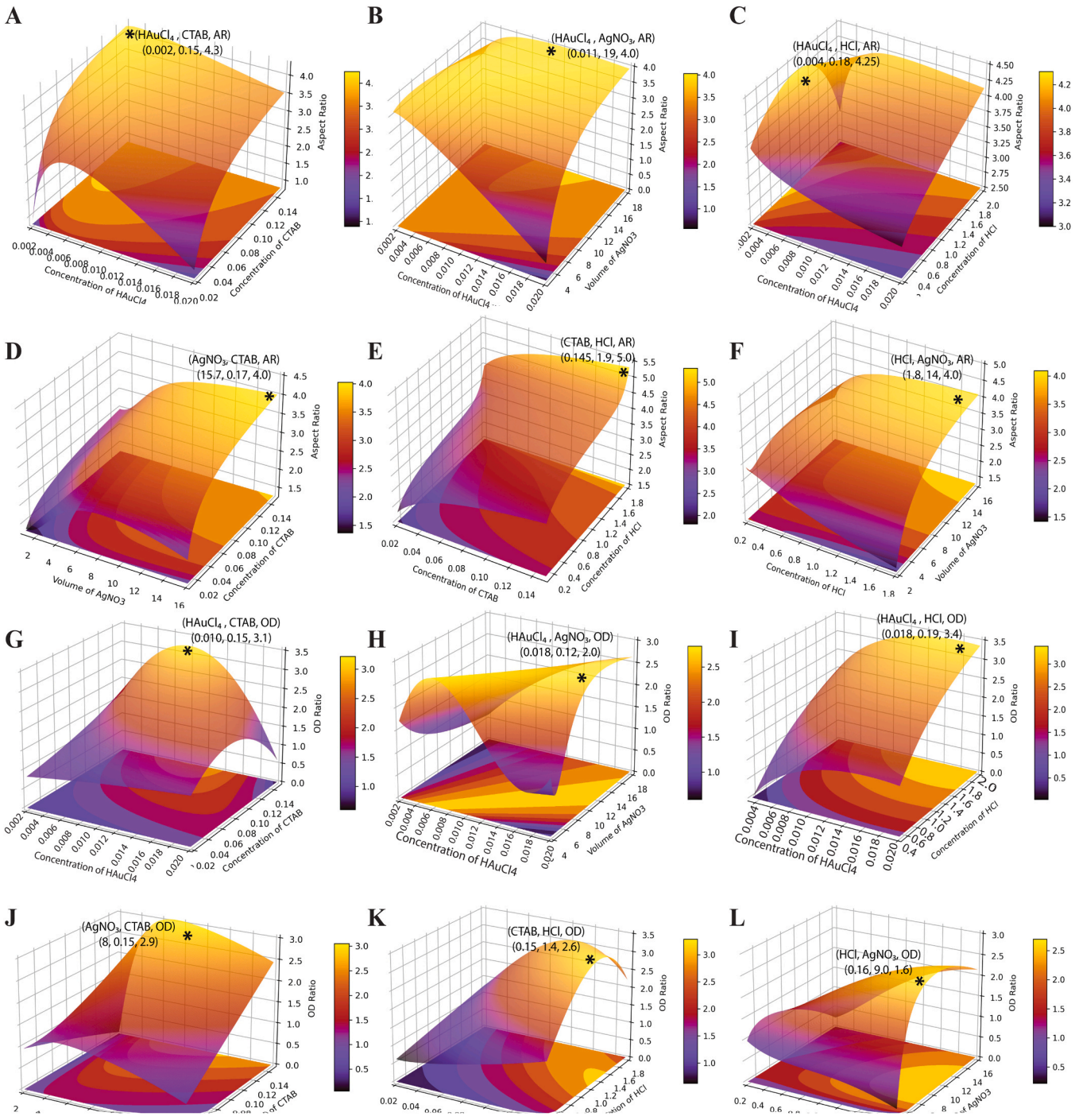

Fig. 5. Robotic HTE platform-executed synthesis with double features (the asterisks signify the global optimal solution), visualized via 3D surface plots of aspect ratio (A-F) and respective OD ratio (G-L), with the obtained experimental data interpreted by algorithmic decision process and conformed with further predictions. The 64 concentration/volumetric/molarity of (A) & (G) $HAuCl_4$/CTAB (B) & (H) $HAuCl_4$/$AgNO_3$ (C) & (I) $HAuCl_4$/HCl (D) & (J) $AgNO_3$/CTAB (E) & (K) CTAB/HCl and (F) & (L) HCl/$AgNO_3$.

extension of individual concentration at the expense of others creates an imbalance of this coordination due to the depletion of either in the reaction solution, leading to multidirectional growths away from targeted Au NRs [65]. The resultant mini-sized Au NRs evidence this with small AR, apparent at low-concentration levels of both precursors, which eventually improved with increasing concentrations (Fig. 5(D)). Amazingly, a similar trend is noted in CTAB/HCL quantitative variation (Table S26), albeit a widely steady increase in Au NRs AR, which tended towards the maximum, as high concentration levels for both were being approached (Fig. 5(E), Table S27). Equally, their ML model showed high prediction accuracy (R^2 >0.9, RMSE <0.01, shown in Fig. 3(C)), which in turn corroborated the visualized 3D surface plots, unveiling the precursor-response dependence. HCl/$AgNO_3$ combination (Table S28) indicates that the majority of Au NRs AR below 2.5 dominate at region comprising low input of Ag ions in the Au growth solution, even with increasing pH (Fig. 5(F), Table S29). However, the upper-right end of the graph projects a further rise in AR, with a higher concentration level for both.

Furthermore, ML-predicted model visualization was used to randomly generate and further extend the dual-descriptors concentration to 96-

concentration level experiments, with each methodology table, obtained results, and data plots (AR and OD ratio) presented in Table S30-S41 and Fig. S7(A-I), respectively. The robotic HTE platform embarked on the extended experimental preparation to ensure the certainty of the obtained 64-concentration level data results and study essential continuity in the nanorod's incremental patterns in the AR and OD ratio. This attempt, at best, resulted in a substantial elevation in the number of Au NRs with LSPRs above 900 nm (aspect ratio $>$ 4.5). An excellent optical density ratio was also obtained.

Another essential attribute of the Au growth solution is the optimal shape homogeneity, denoted as the optical density (OD) ratio, as indicated in (Fig. 5(G-l), Table S(18−29)). Unlike its corresponding AR graphical projection, the best OD ratio from $HAuCl_4$/CTAB pair is centered around and peaked at high CTAB (0.115 M) and moderately above the middle concentration region of $HAuCl_4$ (0.011 M) (Fig. 5(G)). The unique jet-like display in Fig. 5(H) is reminiscent of the coordination among Au and Ag ions, which must be in fixed proportion - in terms of concentration ratio - to optimize a homogenous shape. However, the nanorod production intensified (LSPR peak absorbance) by elevating the input of $HAuCl_4/AgNO_3$ concentration, providing further evidence of the robustness of this DF formulation.

Likewise, Au NRs dominate impurities at the high concentration region of $HAuCl_4$/HCl (Fig. 5(I)). Though to attain a desirable level of quantitative conversion, it has been reported that the stoichiometric ratio of AA to $HAuCl_4$ should not be below approximated equivalence of 1.5. This does not necessarily decide Au NR production or modification but at least optimizes $HAuCl_4$ participation up to above 90 % [66]. Since our default AA concentration is notably within this range, Au NRs optical yield depends on other precursors like HCl to realize full reductant potentials [67]. Also, $AgNO_3$/CTAB utilizes mild-high CTAB concentration, even at high $AgNO_3$ volume, to attain the best OD ratio with a high ML prediction accuracy (R^2 >0.9, RMSE <0.01). From the ML model visualized trend (Fig. 5(J)), we can conclude that the marginal presence of silver ions is enough to accumulate more spherical nanoparticles, while the amount and sizes of Au NRs reduce due to some probable reversal back into nano-spheres [58], even with increasing CTAB.

As for the CTAB/HCl concentration variability, the result stipulated an improved OD ratio across the region of their maximal concentration values but favored more CTAB than HCl (Fig. 5(K)). Finally, HCl and $AgNO_3$, when increasingly combined, produced better homogeneous Au NRs growth solution at the higher concentration region of the former than the latter (Fig. 5(L)). In general, the 96-concentration levels experiments further corroborate the above results, exhibiting different input concentrations that can improve the Au NR yields and homogeneity (Table S30-S41 and Fig. S7 (G-L)).

Robotic HTE platform-executed synthesis with triple-features

In light of the tight and accurate precursor-response correlation hidden in DF ML models, it is scientifically intuitive to extend this method into the Triple-features (TF) combinatorial technique (3 input SMPs are synchronously varied in quantity) and explore reaction dynamics towards optimized Au NRs yields and purity. The automated HTE platform-executed methods and results in a 64-level TF experiment are summarized in Table S42-47, while their ML-generated variations are visually represented in Fig. S8 (A-L). Tight correlations with overall high dimensional prediction accuracy were observed in the 64-level TF experiment with $R^2 > 0.9$, aside from the predicted accuracy of $HAuCl_4$/HCL/CTAB with R^2 of 0.68 (Fig. S3). Although, unlike in DF, TF data plots involve a choice of specific optimal concentration of a determinant precursor, while the two (2) other features are varied. The glaring merit of TF over DF is that the former generates a broader area of improved AR across the whole experimental set-up, devoid of fluctuations, though sometimes slightly less optimized. Nevertheless, TF techniques buttress the opportunity for a diverse selection of Au NRs with specificity.

Suggestively, this trend can be explained by the fact that such combinatorial effects of SMP aid the acceleration reaction pace and, at the same time, balance the equation necessary to elongate Au NRs. This might as well occur in SF, but at a longer time [68], that could eventually climax into deteriorating nanorod growth, evidenced in previous kinetic analyses [67,69]. Incremental input of TF reagents in the reaction compound readily results in a regime characterized by multiple regions of Au NRs yields at the expense of impurities. At lower concentrations, the increment of the OD ratio is sufficiently slow, but unlike DF, exhibited ubiquitously high levels of Au NRs across the region, notwithstanding the superiority of peak AR and OD ratio values in DF.

Subsequently, 96-level experiments ascertain the reproducibility of these combinations with focus and improvements of the optimal region (Table S48-53 and Fig. S9(A-L)). The prediction accuracy increased up to R^2(1) and RMSE (0.0001), with the prediction performance for the $HAuCl_4$/HCL/CTAB TF increasing from 0.68 to 0.99 (OD ratio), only except for its AR in which R^2 reduced from 0.99 to 0.79 (shown in Fig. S4).

We thus confirm that multiple-features combinatorial approaches can optimize the AR and OD ratio of Au NRs predisposed to arbitrary AR and quantity-dependent low absorption levels.

Model experimental validation, corroborated using in-situ and ex-situ morphological characterization

Besides those already analyzed, a close correlation between the in-situ and ex-situ morphological integrity of the synthesized materials can be attained using ML-assisted robotic HTE platform-executable combinatorial approaches. Notably, full width at half maximum (FWHM) can be improved to boost Au NRs optically. This peak resonance quantitation of LSPR linewidths readily evaluates the nanosized gold crystals' homogeneity in their scattering spectra [66,70]. For instance, this optical parameter could be invaluable for the optimization of Au NRs photothermal therapeutically generated heat for cancer treatments or related optical delivery [71], such that the broader the linewidth, the higher the FWHM, the lesser the coherent alignment of irradiated colloidal Au NRs and their overall absorption cross-section vis-à-vis heat dissipated to the surrounding media [71,72]. Hence, we randomly select photothermal-therapy-relevant Au NRs having 808 nm LSPR to evaluate the influence of SF, DF, and TF on size homogeneity (FWHM), an in-situ measurement extracted from non-destructive UV–visible absorption spectroscopy, and further confirmed by TEM (Table 1 and Fig. 6(A-E)).

Counterintuitively, there were remarkable improvements in FWHM of our Au NRs growth via DF and TF, ahead of SF of similar LSPR, despite a report of FWHM to be wavelength-determined [73]. Accordingly, the data obtained from the SF colloid displayed broadband, rather than narrow, because of the variable longitudinal resonances of the individual nanorod component. Outrightly, the selected 808 nm Au NRs from each category reveal a decreased FWHM from an initial 261 in SF to 171 in DF, and 209 in TF, indicating remarkable improvement in the optical uniformity of Au NRs in multiple features approaches (Fig. 6(A)). Noticeably, the DF growth solution exhibited superior size homogeneity

Table 1
Varying input precursor concentration in single-, double- and triple-features techniques, yielding Au nanorods with different absorbance peaks and linewidth, despite similar LSPR at 808 nm.

Parameters	Precursor concentration (M)			UV–VIS generated results			
	CTAB	$HAuCl_4$	HCl	OD (L)	OD Ratio	AR	FWHM
SF	0.1	0.004	1.2	0.482	1.719	4.084	261
DF	0.115	0.007	1.2	1.421	3.170	4.084	171
TF	0.135	0.012	2.05	1.928	2.598	4.084	209

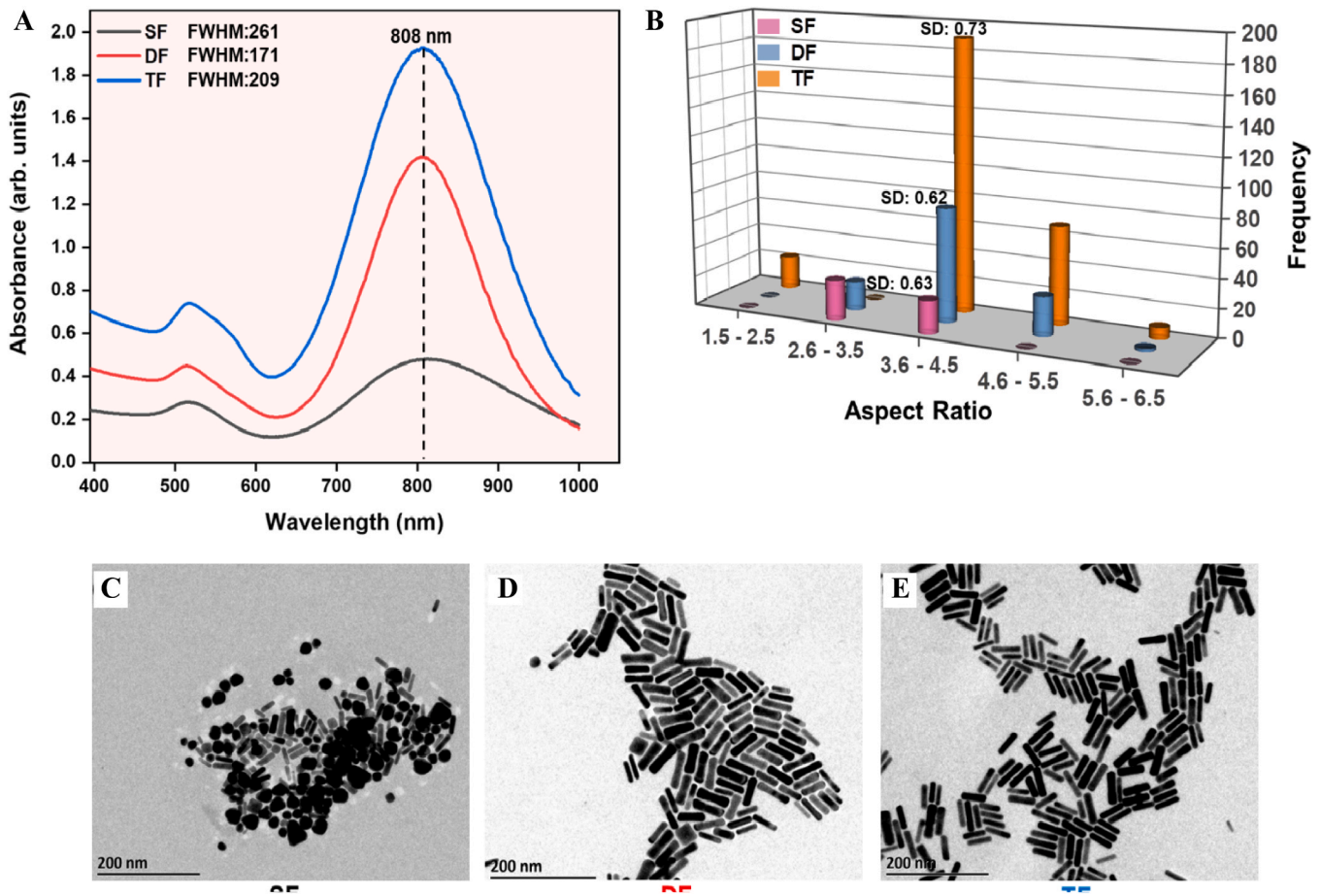

Fig. 6. Combination of in-situ and ex-situ morphological characterization at a specific wavelength of 808 nm by contrasting influence of single-, double- and triple-features techniques (A) Scattering spectra, indicating enhanced absorbance and FWHM beyond SF. (B) 3D histogram juxtaposing their respective aspect ratio. TEM characterized images of Au NR growth samples obtained from (C) Single-Feature, (D) Double-features, and (E) Triple-features techniques. SD denotes the standard deviation.

but less optical density (amount of nanorods produced) than TF. Even though the phenomena that underpin this uniform size distribution of Au NRs are complex, they deserve further in-depth research [60]. It is not far from being insightful to suggest that better FWHM values might be related to relative size distribution via more uniform surface modification through more or lesser synergistic chemicals contributed by the varied SMP in DF and TF techniques.

In corroboration, the ex-situ TEM images indicate hazardous impurities much visible in SF (Fig. 6(C)) were nearly eliminated in DF (Fig. 6 (D)) and TF (Fig. 6(E)), during the growth regime, which arguably contributes towards the realization of similar-sized Au NRs. A 3D histogram reveals the statistical result from these respective TEM images in Fig. 6(B) of contrasting AR calculated from the measured nanorod. The frequency of Au NRs centered around 4.08 AR (equivalent to 808 nm) in TF > DF > SF, with a respective standard deviation of 0.73, 0.62, and 0.63.

We thus confirm that multiple-feature experimental implementations can be used to narrow down heterogeneity for the Au NRs having arbitrary AR. This validates those results obtained from UV−vis spectra, and the adopted AR model is also consistent with TEM results. The detailed statistical data expressing FWHM and dimensions of Au NRs with LSPR at 808 nm across all factor levels are listed in Table 1, which also comprise their length, width, and other quantifications already discussed.

Conclusion

The combination of ML (to recognize patterns hidden in experimental data and utilizing its predictive models to synthesize needed target samples) and robotic HTE platform to form a holistic tool in the exploration, experimentation, and optimization has mutually improved the search over the vast chemical space (as that of Au NRs), accuracy and applicability of developed models towards materials research. To understand the Au NRs synthesis chemical space, we have systematically established existential patterns of ML, guiding ever-improved robotic HTE platform experimental synthesis for seedless fabrication of diverse-sized Au NRs, via tripartite engagement of machine learning models, robotics, and over 1350 pre-collected experimental datasets. Here, a machine learning algorithm was trained and validated to unravel the quantitative and qualitative optimization of Au NRs, backed up by further experiments and TEM characterizations. From our methodological approach, which began with an orthogonal array experiment that led to a combinatorial technique, the resulting robotic HTE platform-operated experimental results ascertained CTAB, $HAuCl_4$, $AgNO_3$, and HCl as the main structure modulating precursors of Au NRs. The synergistic contribution of these agents, in terms of concentrations, was further investigated in double- and triple-feature combinatorial experiments aided by the ML models. This has elevated the practical feasibility of accelerated discovery and scalable control of desirable Au NRs aspect ratio, optical density ratio, and mono-dispersity - derived from individual UV absorption spectra of each growth solution, thereby rendering such highly appealing towards optically-enhanced expansive

application of their optimized versions.

It is believed that such controlled fabrication of seedless Au NRs, having extensively diversified AR, optimizable OD ratio, and other quality-based characterizations such as FWHM, with consistent reproducibility, could unravel an effective platform to fine-tune the physicochemical properties-cum-performances of single-crystal nanomaterials. The guided materials digital synthesis based on the synthesis–structure relationship can be used not only to rationalize the known syntheses and optimize the size and diversity of the available datasets but also to discover novel materials, particularly when fused with theoretical or physical models. This invaluable precursor towards globalization via nanotechnology is a plausible escape to circumvent error-laden human-executed material synthesis. Appropriately, that much avenue was opened to fundamentally decode the systematic contribution from individual reactants, as a structure modulating precursor, towards digital synthesis materials.

Methods

Materials

Hydrogen tetrachloroaurate trihydrate ($HAuCl_4{\cdot}3H_2O$, ≥99.9 %), hydrochloric acid (HCl, 37 %) silver nitrate ($AgNO_3$, 99.8 %), sodium oleate (NaOL, >97 %) and sodium borohydride (NaBH4, 98 %) were made available from Aladdin (China), while hexadecyltrimethylammonium bromide (CTAB, ≥99 %) and L-ascorbic acid (AA, 99 %) were obtained from were purchased from Sigma Aldrich. Ultrapure Milli-Q water (resistivity of 18.25 MΩ cm,) was utilized as solvent in the experiments. All the chemicals used were without any purification utilized as purchased. The chemical plates were beforehand rinsed with deionized water and oven-dried.

Funding

This work was financially supported by the National Natural Science Foundation of China (no. 52173234), Shenzhen Science and Technology Program (JCY20210324102008023), Shenzhen-Hong Kong-Macau Technology Research Program (Type C, SGDX20201103093003 01), Natural Science Foundation of Guangdong Province, China (2022A1515010554), Open Project of Zhengzhou Jishu Institute of AI Science (ZZJSB2023001), Shenzhen Science and Technology Program (ZDSYS20220606100606013) and Wenzhou Smart Energy Key Laboratory Project.

CRediT authorship contribution statement

O.A.M., M.L.A and Z.C. contributed equally to this work. H.Z. conceived the idea. H.Z. acquired the fundings. H.Z., X.Y., Y.L. and Z. Y. supervised the project. O.A.M. designed the HTE experiments and wrote the first draft. O.A.M. and Z.C. performed the HTE experiments and characterizations, analyzed the experimental results. M.L.A, Z.C and Z. W. carried out the machine learning part. C.I.E., W.L., Z.C., B.W., C.W., Z.W., and H.H. helped with characterizations. The final manuscript was written by O.A.M, M.L.A and Z.C. All the authors discussed the results and commented on the manuscript at all stages.

Declaration of Competing Interest

The authors declare that they have no known competing financial interests or personal relationships that could have appeared to influence the work reported in this paper.

Acknowledgements

None.

Appendix A. Supporting information

Supplementary data associated with this article can be found in the online version at doi:10.1016/j.aichem.2023.100028.

References

[1] R.J. Shalloo, S.J.D. Dann, J.N. Gruse, et al., Automation and control of laser wakefield accelerators using Bayesian optimization, Nat. Commun. 11 (1) (2020) 6355.
[2] P. Machillot, C. Quintal, F. Dalonneau, et al., Automated buildup of biomimetic films in cell culture microplates for high-throughput screening of cellular behaviors, Adv. Mater. 30 (27) (2018) 1801097.
[3] H. Zhao, W. Chen, H. Huang, et al., A robotic platform for the synthesis of colloidal nanocrystals, Nat. Synth. 2 (6) (2023) 505–514.
[4] L. Xing, Z. Chen, W. Chen, et al., Robotic platform for accelerating the high-throughput study of silver nanocrystals in sensitive/selective Hg2+ detection, Chem. Eng. J. 466 (143225) (2023).
[5] A. Kusiak, Smart manufacturing must embrace big data, Nature 544 (2017) 23–25.
[6] Z. Zhu, D.W. Hou Ng, H. Park, et al., 3D-printed multifunctional materials enabled by artificial-intelligence-assisted fabrication technologies, Nat. Rev. Mater. 6 (1) (2021) 27–47.
[7] Zhijie Zhu, D.W.H.N. Hyun, S.O.O. Park, Michael C. Mcalpine, 3D-printed multifunctional materials enabled by artificial-intelligence-assisted fabrication technologies, Nat. Rev. Mater. 6 (2021) 27–47.
[8] C. Liu, E. Fujita, Y. Katsura, et al., Machine learning to predict quasicrystals from chemical compositions, Adv. Mater. 33 (36) (2021) 2102507.
[9] F. Lai, Z. Sun, S.E. Saji, et al., Machine Learning-aided crystal facet rational design with ionic liquid controllable synthesis, Small 17 (12) (2021), e2100024.
[10] L. Wu, Z. Xu, Z. Wang, et al., Machine learning accelerated carbon neutrality research using big data—from predictive models to interatomic potentials, in: Sci. China: Technol. Sci, 65, 2022, pp. 2274–2296.
[11] R. Batra, L. Song, R. Ramprasad, Emerging materials intelligence ecosystems propelled by machine learning, Nat. Rev. Mater. 6 (8) (2021) 655–678.
[12] K. Rajan, Materials informatics, Mater. Today 8 (10) (2005) 38–45.
[13] Z. Wang, Z. Sun, H. Yin, et al., Data-driven materials innovation and applications, Adv. Mater. 34 (36) (2022), e2104113.
[14] P. Schwaller, D. Probst, A.C. Vaucher, et al., Mapping the space of chemical reactions using attention-based neural networks, Nat. Mach. Intell. 3 (2) (2021) 144–152.
[15] N.S. Eyke, B.A. Koscher, K.F. Jensen, Toward machine learning-enhanced high-throughput experimentation, Trends Chem. (2021).
[16] J.L. Beckham, K.M. Wyss, Y. Xie, et al., Machine learning guided synthesis of flash graphene, Adv. Mater. 34 (12) (2022) 2106506.
[17] B. Burger, P.M. Maffettone, V.V. Gusev, et al., A mobile robotic chemist, Nature 583 (7815) (2020) 237–241.
[18] S. Steiner, J. Wolf, S. Glatzel, et al., Organic synthesis in a modular robotic system driven by a chemical programming language, Science 363 (6423) (2019) eaav2211.
[19] D. Perera, J.W. Tucker, S. Brahmbhatt, et al., A platform for automated nanomole-scale reaction screening and micromole-scale synthesis in flow, Science 359 (6374) (2018) 429–434.
[20] D. Angelone, A.J.S. Hammer, S. Rohrbach, et al., Convergence of multiple synthetic paradigms in a universally programmable chemical synthesis machine, Nat. Chem. 13 (1) (2021) 63–69.
[21] Zytkow J.M., ZHU J., HUSSAM A.. Automated Discovery in a Chemistry Laboratory; proceedings of the AAAI, F, 1990.
[22] P.G. Katona, A.N. Pappalardo, C.W. Marble, et al., Automated chemistry laboratory, application of a novel time-shared computer system, Proc. IEEE 57 (11) (1969) 2000–2006.
[23] C.G. Enke, Computers in scientific instrumentation, Science 215 (4534) (1982) 785–791.
[24] K. Mathew, J.H. Montoya, A. Faghaninia, et al., Atomate, a high-level interface to generate, execute, and analyze computational materials science workflows, Comput. Mater. Sci. 139 (2017) 140–152.
[25] S.P. Ong, W.D. Richards, A. Jain, et al., Python materials genomics (pymatgen), a robust, open-source python library for materials analysis, Comput. Mater. Sci. 68 (2013) 314–319.
[26] K. Mathew, J.H. Montoya, A. Faghaninia, et al., Atomate, a high-level interface to generate, execute, and analyze computational materials science workflows, Comput. Mater. Sci. 139 (2017) 140–152.
[27] J. Kimmig, S. Zechel, U.S. Schubert, Digital transformation in materials science, a paradigm change in material's development, Adv. Mater. 33 (8) (2021) 2004940.
[28] R. Pollice, Passos Dos, G. Gomes, M. Aldeghi, et al., Data-driven strategies for accelerated materials design, Acc. Chem. Res. 54 (4) (2021) 849–860.
[29] S. Steiner, J. Wolf, S. Glatzel, et al., Organic synthesis in a modular robotic system driven by a chemical programming language, Science 363 (6423) (2019) eaav2211.
[30] H. Yin, Z. Sun, Z. Wang, et al., The data-intensive scientific revolution occurring where two-dimensional materials meet machine learning, Cell Rep. Phys. Sci. 2 (2021) 7.
[31] X. Zhang, Z. Wang, A.M. Lawan, et al., Data-driven structural descriptor for predicting platinum-based alloys as oxygen reduction electrocatalysts, InfoMat (2023), e12406.

[32] R.J. Shalloo, S.J.D. Dann, J.N. Gruse, et al., Automation and control of laser wakefield accelerators using Bayesian optimization, Nat. Commun. 11 (1) (2020) 6355.
[33] L. Wu, Z. Chen, Z. Yuan, et al., Data-driven fine element tuning of halide double perovskite for enhanced photoluminescence, Adv. Opt. Mater. (2023) 2301245.
[34] L. Zhang, K. Xia, Z. Lu, et al., Efficient and facile synthesis of gold nanorods with finely tunable plasmonic peaks from visible to near-IR range, Chem. Mater. 26 (5) (2014) 1794–1798.
[35] X. Huang, I.H. El-Sayed, M.A. El-Sayed, Applications of gold nanorods for cancer imaging and photothermal therapy, Methods Mol. Biol. 624 (2010) 343–357.
[36] Y. Han, Y. Han, J. Sun, et al., Controllable nanoparticle aggregation through a superhydrophobic laser-induced graphene dynamic system for surface-enhanced Raman scattering detection, ACS Appl. Mater. Interfaces 14 (2) (2022) 3504–3514.
[37] M.Y. Tsvetkov, B.N. Khlebtsov, V.A. Khanadeev, et al., SERS substrates formed by gold nanorods deposited on colloidal silica films, Nanoscale Res. Lett. 8 (1) (2013) 1–9.
[38] Bär J. DE Barrosa, D.H. De Camargo, et al., Silicon microchannel-driven raman scattering enhancement to improve gold nanorod functions as a SERS substrate toward single-molecule detection, ACS Appl. Mater. Interfaces 13 (30) (2021) 36482–36491.
[39] L. Xing, Y. Xiahou, X. Zhang, et al., Large-area monolayer films of hexagonal close-packed Au@Ag nanoparticles as substrates for SERS-based quantitative determination, ACS Appl. Mater. Interfaces 14 (11) (2022) 13480–13489.
[40] L. Xing, C. Wang, Y. Cao, et al., Macroscopical monolayer films of ordered arrays of gold nanoparticles as SERS substrates for in situ quantitative detection in aqueous solutions, Nanoscale 13 (35) (2021) 14925–14934.
[41] Q. Zhang, Y. Yu, X. Yun, et al., Multicolor colorimetric sensor for detection of omethoate based on the inhibition of the enzyme-induced metallization of gold nanorods, ACS Appl. Nano Mater. 3 (6) (2020) 5212–5219.
[42] J. Hong, A. Kawashima, N.A. Hamada, Simple fabrication of plasmonic surface-enhanced Raman scattering (SERS) substrate for pesticide analysis via the immobilization of gold nanoparticles on UF membrane, Appl. Surf. Sci. 407 (2017) 440–446.
[43] N. Ullah KHAN, Z. Muhammad, X. LIU, et al., Ultrasensitive detection of exosome using biofunctionalized gold nanorods on a silver-island film, Nano Lett. 21 (13) (2021) 5532–5539.
[44] H.-H. Jeong, E. Choi, E. Ellis, et al., Recent advances in gold nanoparticles for biomedical applications, from hybrid structures to multi-functionality, J. Mater. Chem. B 7 (22) (2019) 3480–3496.
[45] M. Adelt, D.A. Maclaren, D.J. Birch, et al., Morphological changes of silica shells deposited on gold nanorods: implications for nanoscale photocatalysts, ACS Appl. Nano Mater. 4 (8) (2021) 7730–7738.
[46] T.D. Tran, M.T.T. Nguyen, Hoang V. Le, et al., Gold nanoparticles as an outstanding catalyst for the hydrogen evolution reaction, Chem. Commun. 54 (27) (2018) 3363–3366.
[47] R. Ouyang, E. Ahmetcik, C. Carbogno, et al., Simultaneous learning of several materials properties from incomplete databases with multi-task SISSO, J. Phys. Mater. 2 (2) (2019), 024002.
[48] R. Ouyang, S. Curtarolo, E. Ahmetcik, et al., SISSO: a compressed-sensing method for identifying the best low-dimensional descriptor in an immensity of offered candidates, Phys. Rev. Mater. 2 (8) (2018), 083802.
[49] X.U.W. Andersen, M. Reuter, K. Data-Driven, descriptor engineering and refined scaling relations for predicting transition metal oxide reactivity, ACS Catal. 11 (2) (2020) 734–742.
[50] M. Andersen, K. Reuter, Adsorption enthalpies for catalysis modeling through machine-learned descriptors, Acc. Chem. Res. 54 (12) (2021) 2741–2749.
[51] S. Addelman, Recent developments in the design of factorial experiments, J. Am. Stat. Assoc. 67 (337) (1972) 103–111.
[52] E.-S.A. Al-Sherbini, UV–visible light reshaping of gold nanorods, Mater. Chem. Phys. 121 (1–2) (2010) 349–353.
[53] P.L. GAI, M.A. Harmer, Surface atomic defect structures and growth of gold nanorods, Nano Lett. 2 (7) (2002) 771–774.
[54] Y. Wang, Y.F. Li, J. Wang, et al., End-to-end assembly of gold nanorods by means of oligonucleotide–mercury (II) molecular recognition, Chem. Commun. 46 (8) (2010) 1332–1334.
[55] M.S. Vega, F. Brisset, G. Laurent, Optimized silica shell synthesis surrounding gold nanorods for enhanced spectroscopies, Plasmonics 16 (3) (2021) 635–642.
[56] M. Gorbunova, V. Apyari, S. Dmitrienko, et al., Gold nanorods and their nanocomposites: synthesis and recent applications in analytical chemistry, TrAC, Trends Anal. Chem. 130 (2020), 115974.
[57] B. Nikoobakht, M.A. El-Sayed, Preparation and growth mechanism of gold nanorods (NRs) using seed-mediated growth method, Chem. Mater. 15 (10) (2003) 1957–1962.
[58] X. Zhang, N. Tran, T. Egan, et al., Synthesis of homogeneous gold nanorods through the optimized multi-step seed-mediated growth method, J. Phys. Chem. C 125 (24) (2021) 13350–13360.
[59] X. Xu, Y. Zhao, X. Xue, et al., Seedless synthesis of high aspect ratio gold nanorods with high yield, J. Mater. Chem. A 2 (10) (2014) 3528–3535.
[60] A.K. Sahu, A. Das, A. Ghosh, et al., Understanding blue shift of the longitudinal surface plasmon resonance during growth of gold nanorods, Nano Express 2 (1) (2021), 010009.
[61] M.L. Personick, M.R. Langille, J. Zhang, et al., Shape control of gold nanoparticles by silver underpotential deposition, Nano Lett. 11 (8) (2011) 3394–3398.
[62] H. Yuan, W. Ma, C. Chen, et al., Shape and SPR evolution of thorny gold nanoparticles promoted by silver ions, Chem. Mater. 19 (7) (2007) 1592–1600.
[63] L. Nguyen, M. Dass, M.F. Ober, et al., Chiral assembly of gold–silver core–shell plasmonic nanorods on DNA origami with strong optical activity, ACS Nano 14 (6) (2020) 7454–7461.
[64] L.I.U.M. Guyot-Sionnest, Mechanism of silver (I)-assisted growth of gold nanorods and bipyramids, J. Phys. Chem. B 109 (47) (2005) 22192–22200.
[65] E. Piktel, Ł. Suprewicz, J. Depciuch, et al., Varied-shaped gold nanoparticles with nanogram killing efficiency as potential antimicrobial surface coatings for the medical devices, Sci. Rep. 11 (1) (2021) 1–20.
[66] R. Gallagher, X. Zhang, A. Altomare, et al., pH-mediated synthesis of monodisperse gold nanorods with quantitative yield and molecular level insight, Nano Res 14 (4) (2021) 1167–1174.
[67] W. Tong, M.J. Walsh, P. Mulvaney, et al., Control of symmetry breaking size and aspect ratio in gold nanorods: underlying role of silver nitrate, J. Phys. Chem. C 121 (6) (2017) 3549–3559.
[68] N.Z. Md Shah, M. Morsin, R. Sanudin, et al., Effects of growth solutions ageing time to the formation of gold nanorods via two-step approach for plasmonic applications, Plasmonics 15 (2020) 923–932.
[69] K. Park, L.F. Drummy, R.C. Wadams, et al., Growth mechanism of gold nanorods, Chem. Mater. 25 (4) (2013) 555–563.
[70] X. Zhang, R. Gallagher, D. He, et al., pH regulated synthesis of monodisperse penta-twinned gold nanoparticles with high yield, Chem. Mater. 32 (13) (2020) 5626–5633.
[71] Vikas, Raj Kumar, Sanjeev Soni, Investigation of the plasmonic interaction of gold nanoparticles toward plasmonic photothermal therapeutics, Plasmonics 17 (1) (2022) 107–118.
[72] G. González-Rubio, P. Díaz-Núñez, A. Rivera, et al., Femtosecond laser reshaping yields gold nanorods with ultranarrow surface plasmon resonances, Science 358 (6363) (2017) 640–644.
[73] L.-N. Meng, J. Zhu, G.-J. Weng, et al., Optimization of the ultra-narrow plasmonic band width of Pt-coated Au nanorod: the application in refractive index sensing, Physica E (2021), 114996.